Journal of Thermal Analysis and Calorimetry (2021) 143:929–944
https://doi.org/10.1007/s10973-020-09459-4

Significance of nonlinear thermal radiation in 3D Eyring–Powell nanofluid flow with Arrhenius activation energy

Taseer Muhammad[1] · Hassan Waqas[2] · Shan Ali Khan[2] · R. Ellahi[3,4] · Sadiq M. Sait[5]

Received: 20 January 2020 / Accepted: 15 February 2020 / Published online: 4 March 2020

Abstract
In this paper, a mathematical analysis for three-dimensional Eyring–Powell nanofluid nonlinear thermal radiation with modified heat plus mass fluxes is investigated. To enhance the dynamical and physical study of structure, the slip condition is introduced. A Riga plate is employed for avoiding boundary-layer separation to diminish the friction and pressure drag of submarines. To evaluate the heat transfer, the Cattaneo–Christov heat flux model is implemented via appropriate transformation. A comparison between bvp4c results and shooting technique is made. Graphical and numerical illustrations are presented for prominent parameters.

Keywords Eyring–Powell model · Nanofluid · Nonlinear thermal radiation · Activation energy · Heat and mass fluxes · 3D flow

List of symbols

u, v, w	Velocity components
$\mathrm{Re}_x, \mathrm{Re}_y$	Local Reynolds number
Q	Modified Hartmann number
Sc	Schmidt number
Nu_x	Local Nusselt number
K_1	Porosity parameter
Nr	Radiation parameter
$\tilde{T}_\infty$	Ambient temperature
E_1	Activation energy
f', g'	Velocities
$\tilde{C}_f$	Skin friction coefficient
J_0	Current density
q_w	Wall heat flux
D_T	Thermophoretic diffusion coefficient
x, y, z	Coordinate axes
Pr	Prandtl number
N_T	Thermophoresis number
Le	Lewis number
Sh_x	Local Sherwood number
B	Dimensionless parameter
M	Magnetic parameter
$\tilde{T}_f$	Convective surface temperature
N_B	Brownian motion
$\tilde{C}_\infty$	Ambient concentration
δ_c	Time relaxation
h_m	Wall mass flux
M_0	Magnetization magnets
D_B	Brownian diffusion coefficient

Greek symbols

β	Stretching parameter
δ	Heat basis parameter
σ	Chemical reaction parameter
γ	Biot number
λ	Stretching parameter
α_1	Width for magnets and electrodes
δ^*	Electric conductivity
Γ	Material parameter
Ω_E	Thermal relaxation time
ρ	Density
α	Velocity slip parameter
ω	Non-dimensional fluid parameter

✉ R. Ellahi
rahmatellahi@yahoo.com; rellahi@alumni.ucr.edu

[1] Department of Mathematics, College of Science, King Khalid University, Abha 61413, Saudi Arabia

[2] Department of Mathematics, Government College University Faisalabad, Layyah Campus, Faisalabad, Pakistan

[3] Department of Mathematics and Statistics, International Islamic University, Islamabad, Pakistan

[4] Center for Modeling and Computer Simulation, Research Institute, King Fahd University of Petroleum and Minerals, Dhahran 31261, Saudi Arabia

[5] Center for Communications and IT Research, Research Institute, King Fahd University of Petroleum and Minerals, Dhahran 31261, Saudi Arabia

β_0	Magnetic field strength
ϕ	Concentration distribution
θ	Temperature distribution
δ_t	Temperature diffusion
Ω_C	Concentration relaxation time
τ_w	Wall shear stress

Introduction

In recent years, non-Newtonian fluids due to their extensive role in engineering and industrial applications have attracted the attention of a large number of researchers. These include Reiner–Philippoff fluid, Casson fluid, Carreau fluid, micropolar fluid, Prandtl fluid, power law fluid, Eyring–Powell fluid and Prandtl–Eyring fluid. Such fluids can be used in the processing of chemical; that is why, a number of researchers are investigating non-Newtonian fluids in the process of polymers and in chemical engineering. Besides, nanofluids containing small nanomaterial particles like molecules or atoms are ejected in a base fluid [1–20]. Nanofluid is a fluid typical of nanomaterials coined by Choi and Eastman [21]. The modern convection agents have a point of view that a broad range of production and industrial characteristic plays an important role in the heat transfer in such liquids. Due to this fact, nanoparticles have been used in the past decades as attractive agents in the formation of fluids to maximize heat transfer in industrial automation. By controlling the nanoscale stage in the development of practical tools, materials and systems, they make a significant contribution to nanotechnology. These include inertia, Magnus brown absorption, thermophoresis, liquid precipitation and gravity. Boungiorno et al. [22] examined the vital role in the growth of the non-homogenous scientific equilibrium for the convective transportation of nanoparticles with convectional boundaries. He also developed possible slipping tools for Brownian motion and thermophoresis in nanofluids. Powell and Eyring [23] have introduced fluid model called Eyring–Powell fluid. Patel and Timol [24] developed the Eyring–Powell models more efficient and significant as compared to the power law model, but it was rather complex in nature. Simultaneously, concern was to argue that this fluid's dynamic existence is believed to be resulted from the fluids kinetic theory more than its matter-of-fact expression. The fluid model of Eyring-Powell is used to design the manufacturing in material flows. This model also reduces the viscous fluid flow of the Eyring–Powell fluid to a moveable surface at low and high shear concentrations, as investigated by Hayat et al. [25]. Akbar et al. [26] discussed Eyring–Powell magneto-fluid flow numerically past the stretching sheet by employing the finite difference method. As various non-Newtonian fluid system equations are complex as compared to Navier–Stokes equations, obtaining the solutions of these equations is much difficult but more significant due to the simplicity and ease of Eyring–Powell model and vital in chemical engineering processes. Hayat et al. [27] illustrated Eyring–Powell fluid for Newtonian heat and magnetohydrodynamics, and even today, it is of great significance to improve the mathematical modeling of non-Newtonian fluids [28–35]. Eldabe et al. [36] explored Eyring–Powell fluid for MHD within the variable viscosity effects which has been examined in [37]. Islam et al. [38] reported the disturbance of the Eyring–Powell fluid. Akbar and Nadeem [39] argued an endoscope transfer and heating structure of Eyring–Powell fluid. Sirohi et al. [40] examined the fluid flow of Eyring–Powell near a dynamic plate utilizing various techniques. Nadeem et al. [41] discussed the peristaltic flux of Eyring–Powell fluid. The effect of dual stratification by Eyring–Powell has been inspected by Jayachandra et al. [42]. Yoon and Ghajar [43] offered a brief description of the effect of varying large and small viscosities of shear rate by using Powell–Eyring fluid to understand the nature of fluid time range. Agbaje et al. [44] investigated the incompressible nanoflow limits stage of Eyring–Powell. Gailitis and Lielausis [45] invented the Riga electromagnetic actuator surface, which consists of definitely arranged magnets and electrode sets. Ahmad et al. [46] examined the impact of zero normal mass and heat flux on the motion of nanofluid flowing across a Riga layer. The flow problem was determined by two techniques: (1) the shooting method and (2) bvp4c. Iqbal et al. [47] performed the analysis of nanofluid flow to a variable-thick Riga plate with bioconvection, heat convection and mass flow elements within the flow region. Khan et al. [48] investigated Powell–Eyring MHD fluid by considering the elements of thermophysics. The stretching surface with boundary conditions flow of nanofluid is available in [49]. Goodarzi et al. [50] used two types of mixture model and narrow cavity channel to describe the laminar and turbulent nanofluid case flow. Riaz et al. [51] studied the Eyring–Powell fluid for heat and mass transfer. Three-dimensional Eyring–Powell nanofluids through the stretch sheet were proposed by Gireesha et al. [52]. Hayat et al. [53] determined their three-dimensional previous-degree nanofluid flow instead of utilizing the stretching layer to evaluate the thermal influence flow. Hayat et al. [54] reported Maxwell nanofluid with heat transfer source/sink effects for a three-dimensional boundary-layer flow. Hedayati et al. [55] highlighted the nanofluid flow in a channel. Most of these slip systems are similar to the Fukui–Kaneko (FK) slip demarcation flow model [56], the Maxwell first-order boundary slip flow model [57], the nominal injunction slip surface flow model [58] and the second command slip boundary flow method [59]. Kinetic theory for gases is the origin of these models. These models are used in engineering and science problems. In addition, for chemical reaction, the least required energy to reactants is the activation energy. In chemical industry, oil emulsions, water mechanics and food processing play important roles, and due to concentration, a variance in mixture-type mass transfer process happens. Geothermal reservoirs have been studied for exothermic or endothermic reactions with the aid of activation energy, where activation energy plays an important role in alternate convective flows [60]. Techniques of numerical methods of fractional control problem were reported using the Chebyshev polynomial technique by Zhang et al. [61]. Shafique et al. [62] provided the concept of rotating viscoelastic flow by numerical approaches for chemical reactions and activation energy species for convoluted and nonlinear Fokker–Planck formula. Hemeda and Eladdad [63], along with an integrated scheme, provided the concept of an iterative technique. Asadollahi and Esmaeeli [64] studied two-dimensional simulation of condensation liquid behavior on micro-object with moving walls. They found that an increase in Weber number leads to liquid breakup and consequently this mechanism provides an effective way for removing the condensed liquid from micro-devices surfaces. Their presented results reveal the liquid evolutionary performance and breaking up over time which is ultimately a controllable situation for manipulating the walls velocity. Few useful numerical techniques can be seen in [65–67]. Furthermore, Khan et al. [68] inspected non-Fourier heat flux model on viscoelastic fluid. Nadeem and Muhammad [69] studied the flow of heat from Cattaneo–Christov model and its influence on stratification saturated with porous medium. Hayat et al. [70] discussed chemically reactive double stratified stream via Fourier theory of heat change. Salahuddin et al. [71] applied the variable thicknesses of the Cattaneo–Christov experiment on Williamson fluid via stretched sheet. Recently, Cattaneo–Christov model on Powell–Eyring fluid has been discussed by Hayat et al. [72] with variable thermal conductivity. Powell–Eyring fluid study has not been given awide coverage. There is little literature available to support over the extended surface flow of non-Newtonian fluid from the Eyring–Powell. However, using the concept of non-Fick's theory of mass flux and non-Fourier's theory of thermal flux, Eyring–Powell fluid over a Riga plate with nonlinear thermal energy and activation energy has not been discussed yet.

Model

Let us consider a three-dimensional Eyring–Powell nanofluid with nonlinear thermal radiation, activation energy and the non-Fourier heat transfer and non-Fick's mass flux passing over bidirectional stretching sheet as shown in Fig. 1. Let the stretching velocity about x-direction and y-direction be $\tilde{u} = ax$, $\tilde{v} = by$, respectively. The region $z \geq 0$ is occupied by the fluid. Let us consider the temperature and the nanoparticle's concentration $\tilde{T}_{\mathrm{f}}$, $\tilde{C}_{\mathrm{f}}$ are constant and assume that they are better than the ambient high temperature and the concentration $\tilde{T}_{\infty}$, $\tilde{C}_{\infty}$ (Fig. 1).

A three-dimensional Eyring–Powell model of energy and nanoparticle's concentration with activation energy and nonlinear thermal radiation [73, 74] can be expressed by

$$\left(\frac{\partial \tilde{u}}{\partial x} + \frac{\partial \tilde{v}}{\partial y} + \frac{\partial \tilde{w}}{\partial z}\right) = 0, \tag{1}$$

$$\left(\tilde{u}\frac{\partial \tilde{u}}{\partial x} + \tilde{v}\frac{\partial \tilde{u}}{\partial y} + \tilde{w}\frac{\partial \tilde{u}}{\partial z}\right) = \left(\nu + \frac{1}{\rho \Gamma a}\right)\frac{\partial^2 \tilde{u}}{\partial z^2} - \frac{1}{2\rho \Gamma a^3}\left(\frac{\partial \tilde{u}}{\partial z}\right)^2 \frac{\partial^2 \tilde{u}}{\partial z^2} - \frac{\sigma^* B_0^2}{\rho}\tilde{u} - \frac{\nu \varphi}{K^*}\tilde{u} + \frac{\pi j_0 M_0}{8\rho}\exp\left(\frac{-\pi}{\alpha_1}z\right), \tag{2}$$

$$\left(\tilde{u}\frac{\partial \tilde{v}}{\partial x} + \tilde{v}\frac{\partial \tilde{v}}{\partial y} + \tilde{w}\frac{\partial \tilde{v}}{\partial z}\right) = \left(\nu + \frac{1}{\rho \Gamma a}\right)\frac{\partial^2 \tilde{v}}{\partial z^2} - \frac{1}{2\rho \Gamma a^3}\left(\frac{\partial \tilde{v}}{\partial z}\right)^2 \frac{\partial^2 \tilde{v}}{\partial z^2} - \frac{\sigma B_0^2}{\rho}\tilde{v} - \frac{\nu \varphi}{K^*}\tilde{v}, \tag{3}$$

The Fourier and the Fick laws can be expressed as follows:

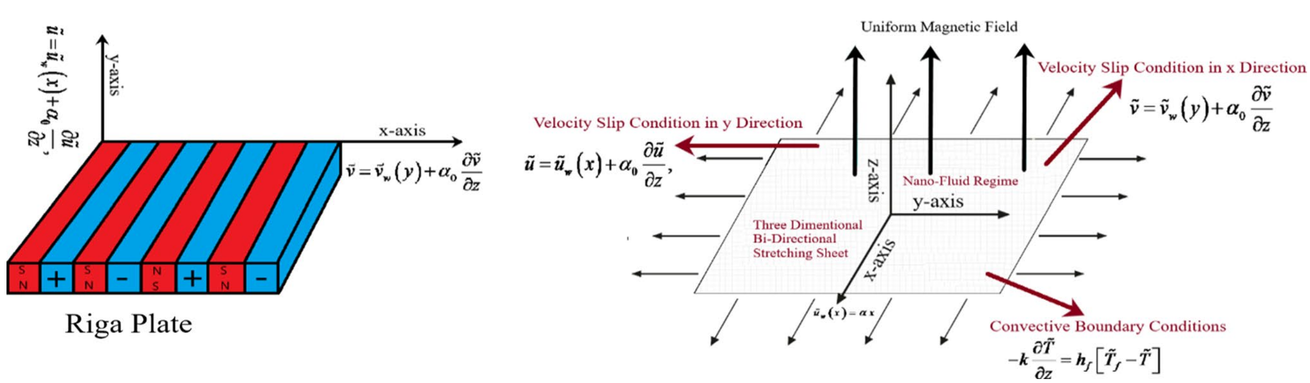

Fig. 1 Flow geometry

$$\vec{q}+\Omega_{\mathrm{E}}\left(\frac{\partial\vec{q}}{\partial t}+\tilde{V}\cdot\nabla\vec{q}-\vec{q}\cdot\nabla\tilde{V}+\left(\nabla\cdot\tilde{V}\right)\vec{q}\right)=-k\nabla\tilde{t}, \tag{4}$$

$$\vec{j}+\Omega_{\mathrm{C}}\left(\frac{\partial\vec{j}}{\partial t}+\tilde{V}\cdot\nabla\vec{j}-\vec{j}\cdot\nabla\tilde{V}+\left(\nabla\cdot\tilde{V}\right)\vec{j}\right)=-D_{\mathrm{B}}\nabla\tilde{C}, \tag{5}$$

$$\begin{aligned}\left(\tilde{u}\frac{\partial\tilde{T}}{\partial x}+\tilde{v}\frac{\partial\tilde{T}}{\partial y}+\tilde{w}\frac{\partial\tilde{T}}{\partial z}+\Omega_{\mathrm{E}}\phi_{\mathrm{E}}\right)&=\alpha\frac{\partial^2\tilde{T}}{\partial z^2}\\&+\tau\left\{D_{\mathrm{B}}\frac{\partial\tilde{C}}{\partial z}\frac{\partial\tilde{T}}{\partial z}+\frac{D_{\mathrm{T}}}{T_\infty}\left(\frac{\partial\tilde{T}}{\partial z}\right)^2\right\}-\frac{1}{(\rho c)_{\mathrm{p}}}\frac{\partial\tilde{q}_{\mathrm{r}}}{\partial z},\end{aligned} \tag{6}$$

$$\begin{aligned}&\left(\tilde{u}\frac{\partial C}{\partial x}+\tilde{v}\frac{\partial\tilde{C}}{\partial y}+\tilde{w}\frac{\partial\tilde{C}}{\partial z}+\Omega_{\mathrm{C}}\phi_{\mathrm{C}}\right)\\&=D_{\mathrm{B}}\left(\frac{\partial^2\tilde{C}}{\partial z^2}\right)+\frac{D_{\mathrm{T}}}{T_\infty}\left(\frac{\partial^2\tilde{T}}{\partial z^2}\right)\\&\quad-Kr^2\left(\tilde{C}-\tilde{C}_\infty\right)\left(\frac{\tilde{T}}{\tilde{T}_\infty}\right)^n\exp\left(\frac{-E_{\mathrm{a}}}{K_1\tilde{T}}\right),\end{aligned} \tag{7}$$

The associated boundary conditions can be given as follows:

$$\begin{aligned}&\tilde{u}=\tilde{u}_{\mathrm{w}}(x)+\alpha_0\frac{\partial\tilde{u}}{\partial z},\\&w=0,-k\frac{\partial\tilde{T}}{\partial z}=h_{\mathrm{f}}\left[\tilde{T}_{\mathrm{f}}-\tilde{T}\right],\\&\text{at } z=0,\tilde{v}=\tilde{v}_{\mathrm{w}}(y)+\alpha_0\frac{\partial\tilde{v}}{\partial z},\end{aligned} \tag{8}$$

$$\tilde{u}\to 0,\tilde{v}\to 0,\tilde{T}\to\tilde{T}_\infty,\tilde{C}\to\tilde{C}_\infty,z\to\infty. \tag{9}$$

Radiative heat flux can be addressed by

$$\tilde{q}_{\mathrm{r}}=-\frac{4\sigma^*}{3k^*}\frac{\partial\tilde{T}^4}{\partial z}=-\frac{16\sigma^*\tilde{T}^3}{3k^*}\frac{\partial\tilde{T}}{\partial z}. \tag{10}$$

Substituting expression (10) in Eq. (6), we get,

$$\begin{aligned}&\left(\tilde{u}\frac{\partial\tilde{T}}{\partial x}+\tilde{v}\frac{\partial\tilde{T}}{\partial y}+\tilde{w}\frac{\partial\tilde{T}}{\partial z}+\Omega_{\mathrm{E}}\phi_{\mathrm{E}}\right)\\&=\alpha\frac{\partial^2\tilde{T}}{\partial z^2}+\tau\left\{D_{\mathrm{B}}\frac{\partial\tilde{C}}{\partial z}\frac{\partial\tilde{T}}{\partial z}+\frac{D_{\mathrm{T}}}{T_\infty}\left(\frac{\partial\tilde{T}}{\partial z}\right)^2\right\}\\&\quad+\frac{16\sigma^*}{3k^*(\rho c)_{\mathrm{p}}}\frac{\partial}{\partial z}\left(\tilde{T}^3\frac{\partial\tilde{T}}{\partial z}\right),\end{aligned} \tag{11}$$

where

$$\begin{aligned}\phi_{\mathrm{E}}=&\,\tilde{u}^2\frac{\partial^2\tilde{T}}{\partial x^2}+\tilde{v}^2\frac{\partial^2\tilde{T}}{\partial y^2}+\tilde{w}^2\frac{\partial^2\tilde{T}}{\partial z^2}\\&+2\tilde{u}\tilde{v}\frac{\partial^2\tilde{T}}{\partial x\partial y}+2\tilde{v}\tilde{w}\frac{\partial^2\tilde{T}}{\partial y\partial z}+2\tilde{u}\tilde{w}\frac{\partial^2\tilde{T}}{\partial x\partial z}\\&+\left(\begin{array}{c}\tilde{u}\frac{\partial\tilde{u}}{\partial x}+\tilde{v}\frac{\partial\tilde{u}}{\partial y}\\+\tilde{w}\frac{\partial\tilde{u}}{\partial z}\end{array}\right)\frac{\partial\tilde{T}}{\partial x}\\&+\left(\tilde{u}\frac{\partial\tilde{v}}{\partial x}+\tilde{v}\frac{\partial\tilde{v}}{\partial y}+\tilde{w}\frac{\partial\tilde{v}}{\partial z}\right)\frac{\partial\tilde{T}}{\partial y}\\&+\left(\tilde{u}\frac{\partial\tilde{w}}{\partial x}+\tilde{v}\frac{\partial\tilde{w}}{\partial y}+\tilde{w}\frac{\partial\tilde{w}}{\partial z}\right)\frac{\partial\tilde{T}}{\partial z},\end{aligned} \tag{12}$$

$$\begin{aligned}\phi_{\mathrm{C}}=&\,\tilde{u}^2\frac{\partial^2\tilde{C}}{\partial x^2}+\tilde{v}^2\frac{\partial^2\tilde{C}}{\partial y^2}+\tilde{w}^2\frac{\partial^2\tilde{C}}{\partial z^2}+2\tilde{u}\tilde{v}\frac{\partial^2\tilde{C}}{\partial x\partial y}+2\tilde{v}\tilde{w}\frac{\partial^2\tilde{C}}{\partial y\partial z}\\&+2\tilde{u}\tilde{w}\frac{\partial^2\tilde{C}}{\partial x\partial z}+\left(\begin{array}{c}\tilde{u}\frac{\partial\tilde{u}}{\partial x}+\tilde{v}\frac{\partial\tilde{u}}{\partial y}\\+\tilde{w}\frac{\partial\tilde{u}}{\partial z}\end{array}\right)\frac{\partial\tilde{C}}{\partial x}\\&+\left(\tilde{u}\frac{\partial\tilde{v}}{\partial x}+\tilde{v}\frac{\partial\tilde{v}}{\partial y}+\tilde{w}\frac{\partial\tilde{v}}{\partial z}\right)\frac{\partial\tilde{C}}{\partial y}+\left(\tilde{u}\frac{\partial\tilde{w}}{\partial x}+\tilde{v}\frac{\partial\tilde{w}}{\partial y}+\tilde{w}\frac{\partial\tilde{w}}{\partial z}\right)\frac{\partial\tilde{C}}{\partial z}.\end{aligned} \tag{13}$$

Let us introduce the following transformation:

$$\begin{aligned}&\eta=\sqrt{\frac{a}{v}z^2},\tilde{u}=axf'(\eta),\tilde{v}=ayg'(\eta),\tilde{w}=-\sqrt{av}(f(\eta)+g(\eta)),\\&\theta(\eta)=\frac{\tilde{T}-\tilde{T}_\infty}{\tilde{T}_{\mathrm{f}}-\tilde{T}_\infty},\phi(\eta)=\frac{\tilde{C}-\tilde{C}_\infty}{\tilde{C}_{\mathrm{w}}-\tilde{C}_\infty}.\end{aligned} \tag{14}$$

Applying similarity transformation to the governing equation, the nonlinear dimensional expressions are reduced to the following expressions:

$$\begin{aligned}&\left(1+\omega-\omega f''(\eta)\right)f'''(\eta)+(f(\eta)+g(\eta))f''(\eta)\\&\quad-K_1f'(\eta)-\left(f'(\eta)\right)^2+Qe^{-B\eta}=0,\end{aligned} \tag{15}$$

$$\begin{aligned}&\left(1+\omega-\omega g''(\eta)\right)g'''(\eta)+(f(\eta)+g(\eta))g''(\eta)\\&\quad-K_1g'(\eta)-\left(g'(\eta)\right)^2=0,\end{aligned} \tag{16}$$

$$\begin{aligned}&\left(1+\varepsilon_1\theta\right)\theta''+\left[\frac{4}{3}N_{\mathrm{r}}\left(1+\left(\theta_{\mathrm{w}}-1\right)\theta\right)^3\right]\theta''\\&\quad+\left[\varepsilon_1+\left(1+\left(\theta_{\mathrm{w}}-1\right)\theta\right)^2\left(4N_{\mathrm{r}}\left(\theta_{\mathrm{w}}-1\right)\right)\theta'^2\right]\\&\quad+\Pr\left(f(\eta)+g(\eta)\right)\theta'(\eta)+N_{\mathrm{B}}\theta'(\eta)\phi'(\eta)\\&\quad+N_{\mathrm{T}}\left(\theta'(\eta)\right)^2-\delta_{\mathrm{t}}(f+g)\left(f'+g'\right)\theta'\\&\quad+(f+g)^2\theta''=0,\end{aligned}\tag{17}$$

$$\begin{aligned}&\phi''(\eta)+S_{\mathrm{c}}(f(\eta)+g(\eta))\phi'(\eta)+\frac{N_{\mathrm{T}}}{N_{\mathrm{B}}}\theta''(\eta)\\&\quad-S_{\mathrm{c}}\sigma(1+\delta\theta)^n\exp\left(\frac{-E_1}{1+\delta\theta}\right)\phi(\eta)\\&\quad-\delta_{\mathrm{c}}(f+g)\left(f'+g'\right)\phi(\eta)+(f+g)^2\phi''(\eta)=0,\end{aligned}\tag{18}$$

$$f(0)=g(0)=0,f(0)=1+\alpha f''(0),g'(0)=\lambda+\alpha g''(0),\tag{19}$$

$$f'(\eta)=0,g'(\eta)=0,\theta(\eta)=0,\phi(\eta)=0\text{ as }\eta\to 0,\tag{20}$$

where the porosity parameter is K_1, dimensionless constant B, customized Hartmann number Q, radiation parameter N_{r}, non-dimensional fluid parameter ω, Prandtl number Pr, velocity slip parameter α, Schmidt number Sc, thermophoresis number N_{T}, Brownian motion N_{B}, activation energy E_1, chemical reaction parameter σ, heat parameter δ, Biot number γ, recreation for temperature diffusion δ_{t} and time relaxation for mass diffusion δ_{c}, which are expressed as follows:

$$\begin{aligned}&E_1=\frac{E_{\mathrm{a}}}{k_1T_\infty},\quad K_1=\frac{\sigma^*B_0^2}{a\rho_{\mathrm{f}}}+\frac{v_f\varphi}{aK^*},\quad \Pr=\frac{v}{a},\\&\mathrm{N_B}=\frac{\tau D_{\mathrm{B}}}{v}\left(\tilde{C}_{\mathrm{w}}-\tilde{C}_\infty\right),\quad \alpha=\alpha_0\left(\frac{v}{a}\right)^{-\frac{1}{2}},\\&\gamma=\frac{h}{k}\sqrt{\frac{v}{a}},\quad \lambda=\frac{b}{a},\quad \sigma=\frac{k_{\mathrm{r}}^2}{a},\quad \delta=\frac{b^3x^2}{2vc^2},\\&\mu=v\rho,\quad N_{\mathrm{T}}=\frac{\tau D_{\mathrm{T}}}{vT_\infty}\left(\tilde{T}_{\mathrm{f}}-\tilde{T}_\infty\right),\quad \omega=\frac{1}{\mu\Gamma a},\\&N_{\mathrm{r}}=\frac{4\sigma T_\infty^3}{k^*k},\quad S_{\mathrm{c}}=\frac{\alpha}{D_{\mathrm{B}}},\quad \delta_{\mathrm{t}}=b\lambda_{\mathrm{E}},\quad \delta_{\mathrm{c}}=b\lambda_{\mathrm{C}},\\&Q=\frac{\pi M_0J_0}{8\rho a^2x},\quad B=\frac{\pi}{\alpha_1}\left(\sqrt{\frac{v}{a}}\right).\end{aligned}\tag{21}$$

To drive the skin friction coactive $\tilde{C}_{\mathrm{f}}$, the Newton method is used. The Fourier law is implemented to find the value of the Nusselt number $\mathrm{Nu_x}$. Also to find the value of local Sherwood number $\mathrm{Sh_x}$, the Fick's laws have been utilized. Finally, the quantities of interest can be written as:

$$\begin{aligned}&C_{\mathrm{fx}}=\frac{\tau_{\mathrm{wx}}}{\rho U_{\mathrm{u}}^2},\quad C_{\mathrm{fy}}=\frac{\tau_{\mathrm{wy}}}{\rho U_{\mathrm{w}}^2},\quad \mathrm{Nu_x}=\frac{xq_{\mathrm{w}}}{k_1\left(\tilde{T}_{\mathrm{w}}-\tilde{T}_\infty\right)},\\&\mathrm{Sh_x}=\frac{xq_{\mathrm{m}}}{k_1\left(\tilde{C}_{\mathrm{w}}-\tilde{C}_\infty\right)}.\end{aligned}\tag{22}$$

τ_{wx}, τ_{wy} are the barrage shear stress next to x-axis and y-axis, respectively, which are defined as:

$$\tau_{\mathrm{wx}}=\mu\left(\frac{\delta\tilde{u}}{\delta z}+\frac{\delta\tilde{w}}{\delta x}\right)_{z=0},\ \tau_{\mathrm{wy}}=\mu\left(\frac{\delta\tilde{v}}{\delta z}+\frac{\delta\tilde{w}}{\delta y}\right)_{z=0},\tag{23}$$

where

$$h_{\mathrm{m}}=-D_{\mathrm{B}}\left(\frac{\delta\tilde{C}}{\delta z}\right)_{z=0},\quad h_{\mathrm{m}}=-k\left(\frac{\delta\tilde{T}}{\delta z}\right)_{z=0}.\tag{24}$$

Substituting (22) to (24), we get

$$\begin{aligned}&C_{\mathrm{fx}}\mathrm{Re}_{\mathrm{x}}^{0.5}=-f''(0),\quad C_{\mathrm{fy}}\mathrm{Re}_{\mathrm{y}}^{0.5}=-g''(0),\\&\frac{\mathrm{Nu_x}}{\mathrm{Re}_{\mathrm{x}}^{0.5}}=-\theta'(0),\quad \frac{\mathrm{Sh_x}}{\mathrm{Re}_{\mathrm{x}}^{0.5}}=-\phi'(0).\end{aligned}\tag{25}$$

Here, the local Reynolds number on relied stretching velocity, local Sherwood number and local Nusselt number are denoted, respectively, as $\mathrm{Re_x}$, $\mathrm{Re_y}$, $\mathrm{Sh_x}$, $\mathrm{Nu_x}$.

Numerical procedure

The set of nonlinear coupled differential equations with dimensionless boundaries as described in (14)–(19) have been solved to find numerical results for velocity, high temperature and concentration by utilizing Lobatto IIIa finite difference shooting method bvp4c via computational software MATLAB.

Let us consider

$$
\left.\begin{aligned}
&f = l_1, \frac{\mathrm{d}f}{\mathrm{d}\eta} = l_2, \frac{\mathrm{d}^2 f}{\mathrm{d}\eta^2} = l_3, \frac{\mathrm{d}^3 f}{\mathrm{d}\eta^3} = l_3', g = l_4,\\
&\frac{\mathrm{d}g}{\mathrm{d}\eta} = l_5, \frac{\mathrm{d}^2 g}{\mathrm{d}\eta^2} = l_6, \frac{\mathrm{d}^3 g}{\mathrm{d}\eta^3} = l_6', \theta = l_7, \frac{\mathrm{d}\theta}{\mathrm{d}\eta} = l_8,\\
&\frac{\mathrm{d}^2\theta}{\mathrm{d}\eta^2} = l_8', \phi = l_9, \phi' = l_{10}, \phi'' = l_{10}',\\
&l_3' = \frac{1}{(1+\omega-\omega l_3)} - \left(\left(l_1+l_4\right)l_3 + K_1 l_2 + l_2^2 + Qe^{-B\eta}\right),\\
&l_6' = \frac{1}{(1+\omega-\omega l_6)}\left((l_1+l_4)l_6 + k_1 l_5 + l_5^2\right),\\
&l_8' = \frac{1}{\left(1+\varepsilon_1 l_7 + \left(l_1+l_4\right)^2\right)\left(\frac{4}{3}\left(N_r\left(1+\left(\theta_w-1\right)+l_7\right)^3\right)\right)}\begin{bmatrix} -\varepsilon_1 - \left(1+\left(\theta_w-1\right)l_7\right)^2\left(4N_r\left(\theta_w-1\right)\right)l_8^2 \\ -P_r\left[\left(l_1+l_4\right)l_8\right] - N_B l_8 l_{10} - N_T l_8^2 \\ +\delta_t\left(l_1+l_4\right)\left(l_2+l_5\right)l_8 \end{bmatrix},\\
&l_{10}' = \frac{1}{\left(1+\left(l_1+l_4\right)^2\right)}\left(-S_c\left(l_1+l_4\right)l_{10} - \frac{N_T}{N_B}l_8' + S_c\sigma\left(1+\delta l_7\right)^n \exp\left(\frac{-E_1}{1+\delta l_7}\right)l_9 + \delta_c\left(l_1+l_4\right)\left(l_2+l_5\right)l_9\right),\\
&l_1(0) = l_4(0) = 0, l(0) = 1+\alpha l_3(0), l_5(0) = \lambda + \alpha l_6(0),\\
&l_8(0) = -\gamma\left(1-l_7(0)\right),\ l_9(0) = 1,\ \text{at}\ z = 0\\
&l_2(\eta) = 0,\ l_5(\eta) = 0, l_7(\eta) = 0, l_9(\eta) = 0\ \text{as}\ \eta \to 0
\end{aligned}\right\} \quad (26)
$$

Discussion

The 3D Eyring–Powell fluid through a stretching slip with activation energy and velocity slip for different parameters is sketched in Figs. 2–32. Figure 2 demonstrates the combined effects of porosity and magnetic parameter K_1 on f'. It is seen that velocity decreases with higher K_1. Actually, by enhancing the magnetic parameter, the Lorentz forces or struggle forces increase, and due to this reason, the flow of fluid slows down or components of velocity profile decline in fluid. Figure 3 illustrates the effects of K_1 on g'. It is experiential that with the higher values of K_1, velocity component g' reduces. In Fig. 4, the effect of K_1 on temperature distribution θ' is shown. It is noted that temperature distribution θ' boosts up when K_1 is increased. In Fig. 5, the exploration impacts of K_1 on volumetric concentration ϕ' are depicted. The volumetric concentration ϕ' increases with higher K_1. Figure 6 shows the impacts of velocity profile f' on modified Hartmann number Q. It is seen that the velocity is enhanced by higher values of Q. Physically, increasing modified Hartmann number Q leads to the conflicting

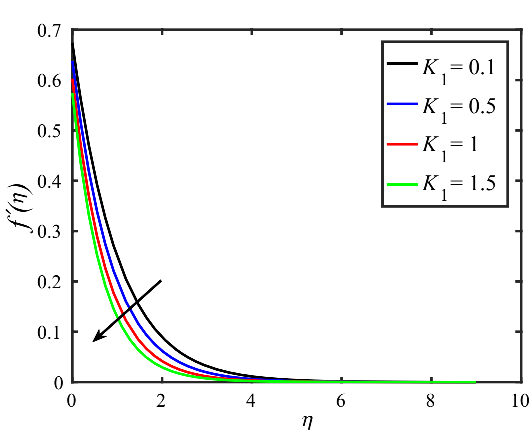

Fig. 2 Profile of $f'(\eta)$ against K_1

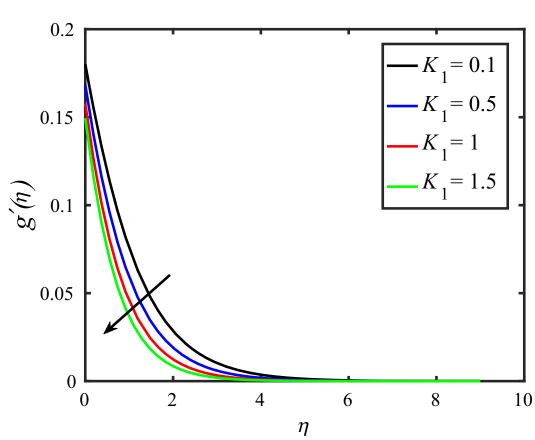

Fig. 3 Profile of $g'(\eta)$ against K_1

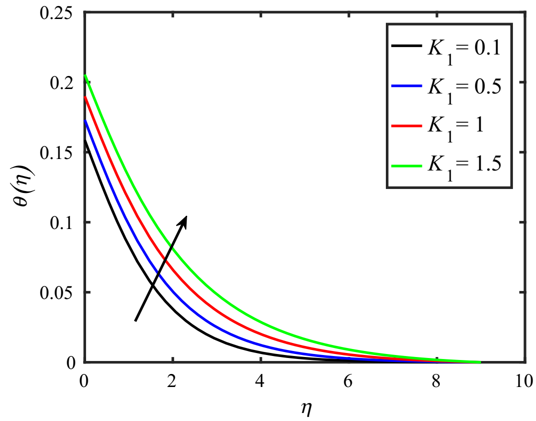

Fig. 4 Profile of $\theta(\eta)$ against K_1

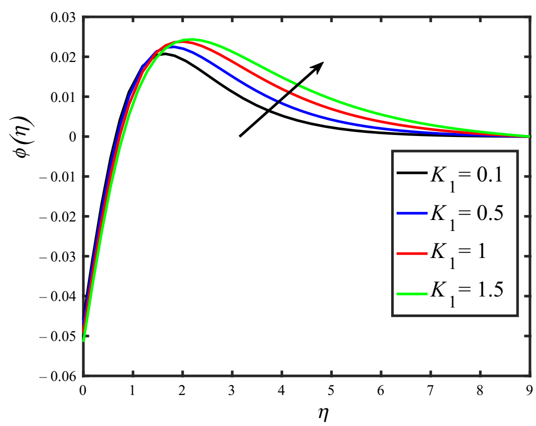

Fig. 5 Profile of $\phi(\eta)$ against K_1

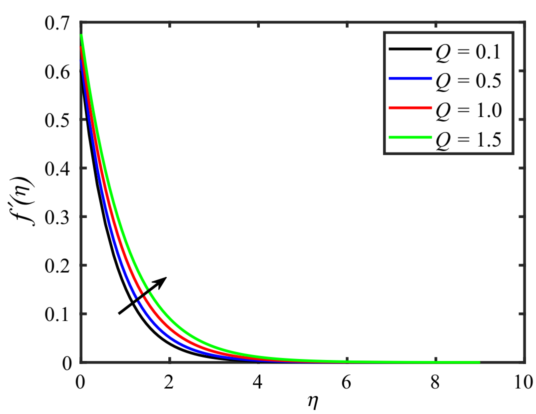

Fig. 6 Profile of $f'(\eta)$ against Q

behavior with the magnetic parameter as observed previously. Higher modified Hartmann number Q values raise the magnetization flanked by the plates, which ultimately assist in accelerating the flow, i.e., the reverse influence to Lorentz

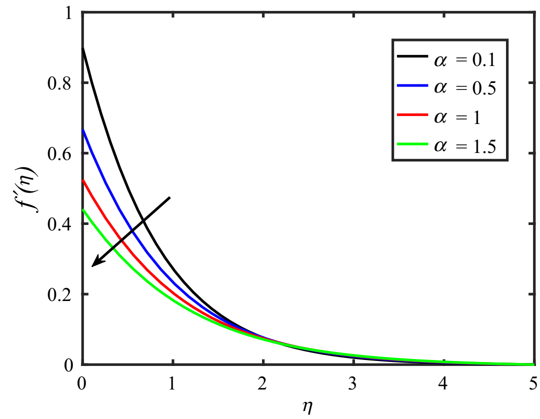

Fig. 7 Profile of $f'(\eta)$ against α

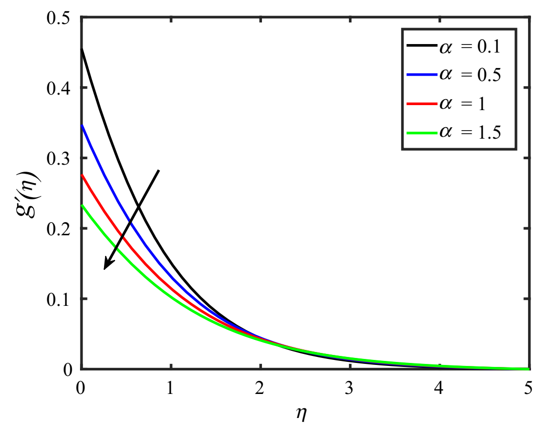

Fig. 8 Profile of $g'(\eta)$ against α

magnetic pull force connected with the magnetic field. This characteristic is exclusively linked with Riga plates. Therefore, velocities are decreased for the situation where the modified Hartmann number Q disappears, and the Riga plate becomes a straight plate in this situation. Figure 7 illustrates the velocity profile for slip parameter α. The velocity profile f' decreases for higher value of α. In Fig. 8, the consequence of α on velocity component g' is depicted. It is noticed that the velocity component g' decreases when α is increased. In Fig. 9, the effects of α on temperature θ are shown in which an increase in α causes a rise in θ. Figure 10 illustrates the effects of α on volumetric concentration ϕ. It is clearly seen that an increase in α causes a reduction in ϕ. Figure 11 shows the stretching parameter β on velocity report f' where reduction in velocity f' is observed with increasing β. Figure 12 reveals the variations of g' for altering principles of β. Augmentation in stretching parameter β leads to a faster pressure group which causes an increase in velocity. Figure 13 represents the graph of stretching parameter β against heat distribution θ. It is exposed that θ decreases with higher

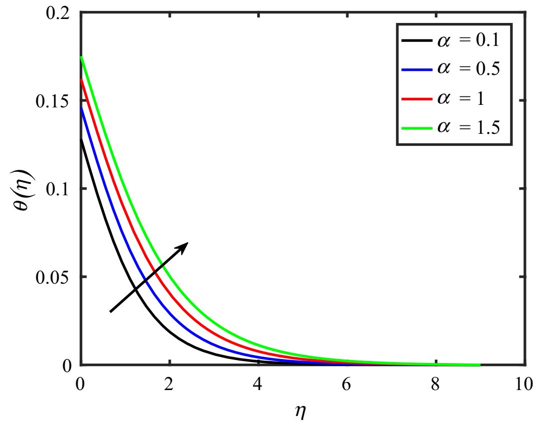

Fig. 9 Profile of $\theta(\eta)$ against α

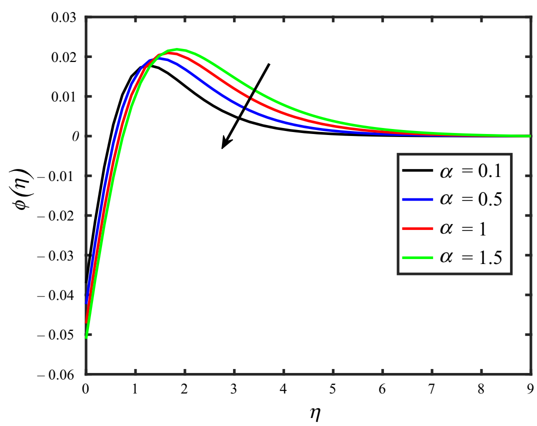

Fig. 10 Profile of $\phi(\eta)$ against α

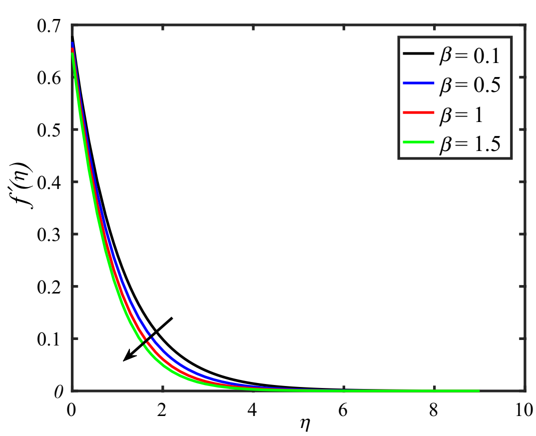

Fig. 11 Profile of $f'(\eta)$ against β

β. Figure 14 represents the volume friction ϕ' via stretching parameter β in which volume friction ϕ' reduces by increasing β. Figures 15 and 16 illustrate the effect of Biot number

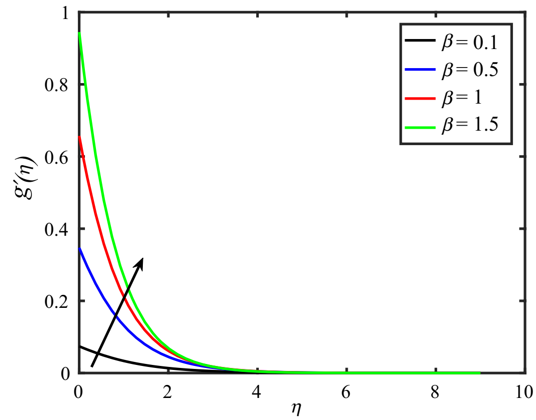

Fig. 12 Profile of $g'(\eta)$ against β

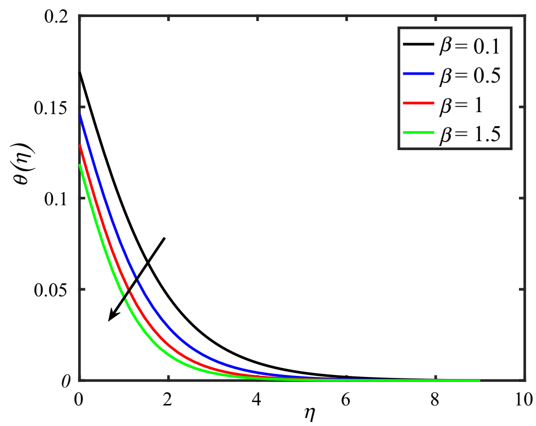

Fig. 13 Profile of $\theta(\eta)$ against β

(γ) on the temperature distribution θ and volumetric concentration profile φ, respectively. It is seen that Biot number γ is directly proportional to the temperature and volumetric concentration profile. Figure 17 shows the witness that thermal distribution increases when one increased the radiation parameter. Physically, one can say that the radiation parameter increases the heat energy between the particles of fluid. It charges them up. Thus, the heat boosts up with the addition of radiation. In Fig. 18, we see that the radiationparameter N_r has direct influence on concentration ϕ. It clearly reveals that the enhancement in radiation parameter N_r enhances its volume friction ϕ. Obviously, the phenomenon in which fluid particles get thermal heat energy has a prominent impact on temperature and volume friction. Figure 19 demonstrates Prandtl Pr for temperature coefficient. It is perceived that temperature behavior has an opposite trend with increasing Pr. Physically, a rise in Prandtl Pr causes low heat penetration, which causes a decrease in the thickness of thermal boundary layer. Figure 20 displays the part

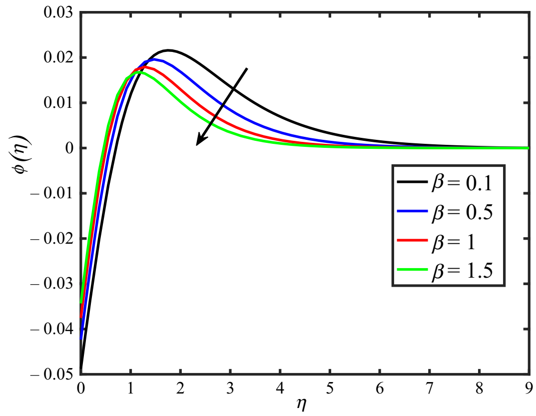

Fig. 14 Profile of $\phi(\eta)$ against β

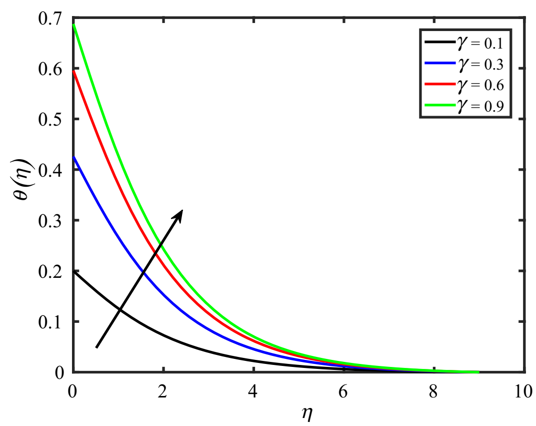

Fig. 15 Profile of $\theta(\eta)$ against γ

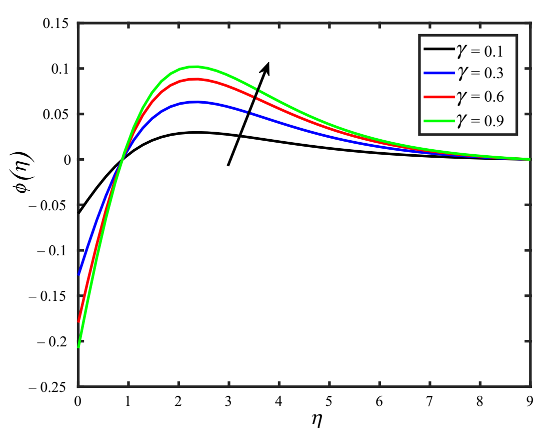

Fig. 16 Profile of $\phi(\eta)$ against γ

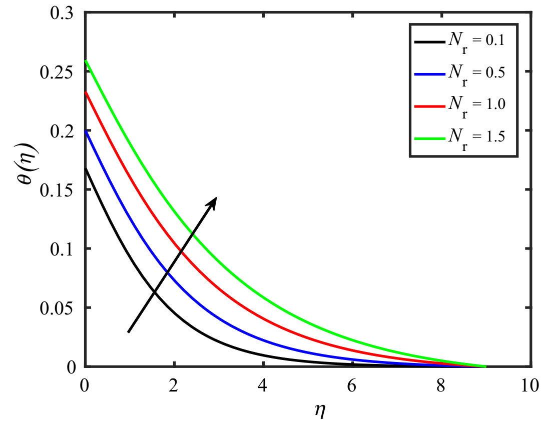

Fig. 17 Profile of $\theta(\eta)$ against N_r

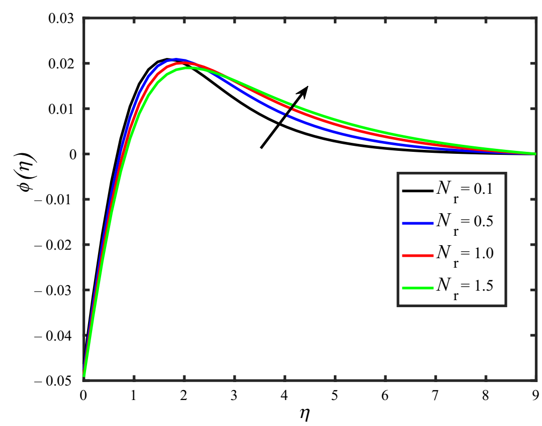

Fig. 18 Profile of $\phi(\eta)$ against N_r

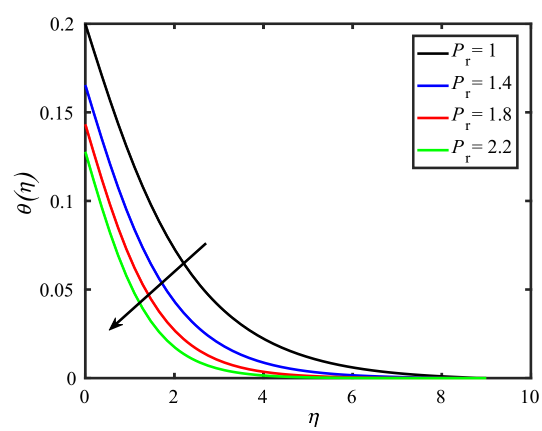

Fig. 19 Profile of $\theta(\eta)$ against Pr

of Pr on concentration; here, Pr is inversely proportional to the concentration trend , which suggests that concentration decreases with increasing Pr. Figures 21 and 22 reveal the consequence of thermophoresis number N_t for temperature distribution θ as well as volume friction of nanoparticles ϕ, respectively. It is detected that a rise in the aspect of

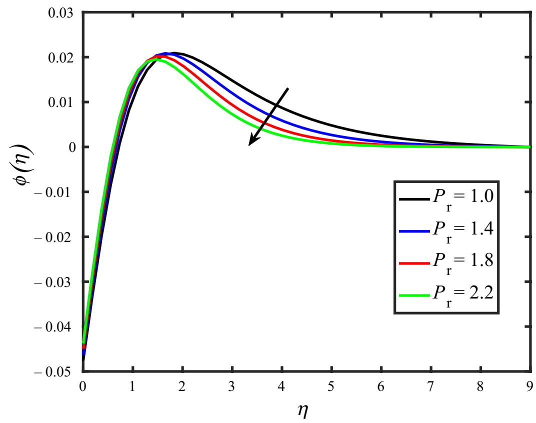

Fig. 20 Profile of $\phi(\eta)$ against Pr

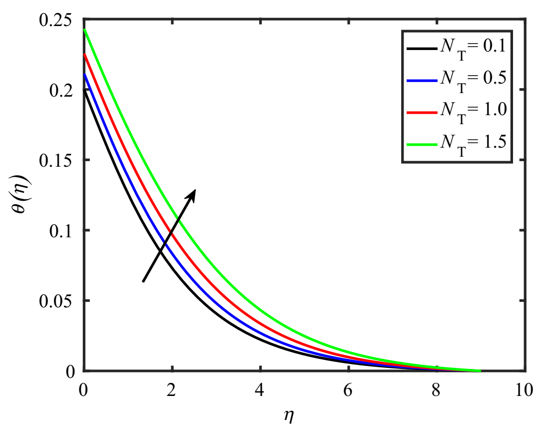

Fig. 21 Profile of $\theta(\eta)$ against N_T

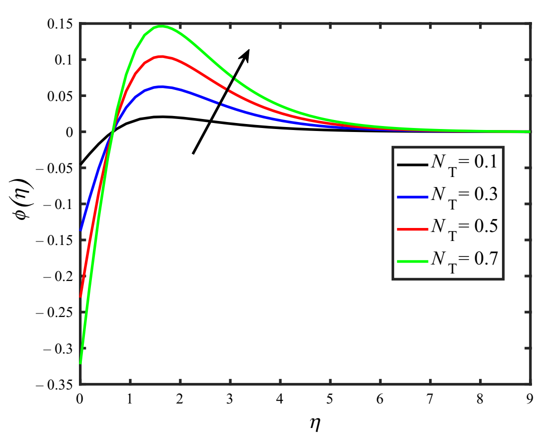

Fig. 22 Profile of $\phi(\eta)$ against N_T

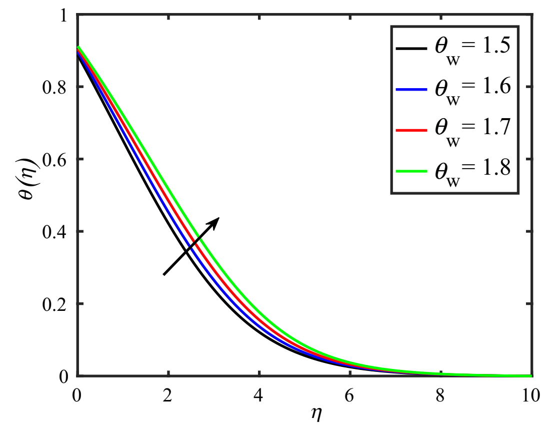

Fig. 23 Profile of $\theta(\eta)$ against θ_n

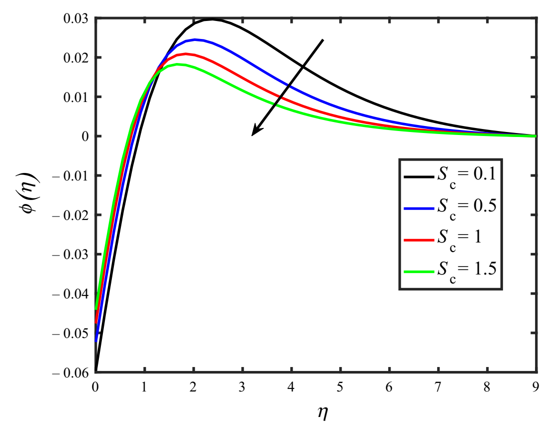

Fig. 24 Profile of $\phi(\eta)$ against S_c

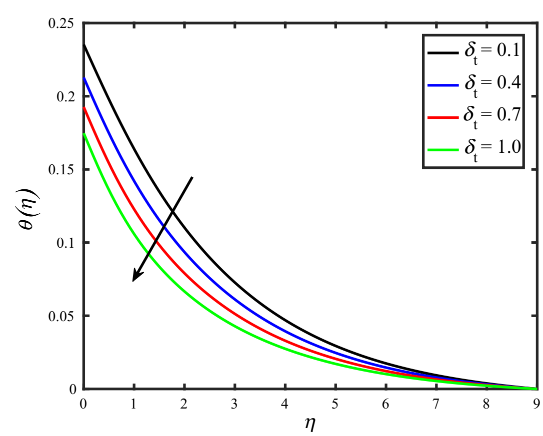

Fig. 25 Profile of $\theta(\eta)$ against δ_t

thermophoresis number N_t results in the rise in temperature and volume friction. Figure 23 visualizes the effect of temperature ratio parameter θ_n on temperature sharing θ in which temperature distribution is boosted up with an increment in temperature relative amount of parameter θ_n. Figure 24 shows the blow of Schmidt number S_c over ϕ in

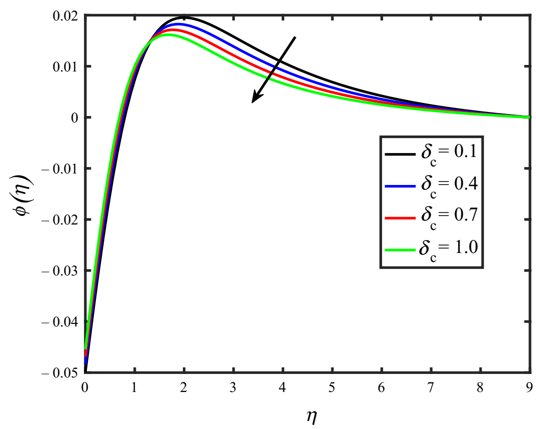

Fig. 26 Profile of $\phi(\eta)$ against δ_c

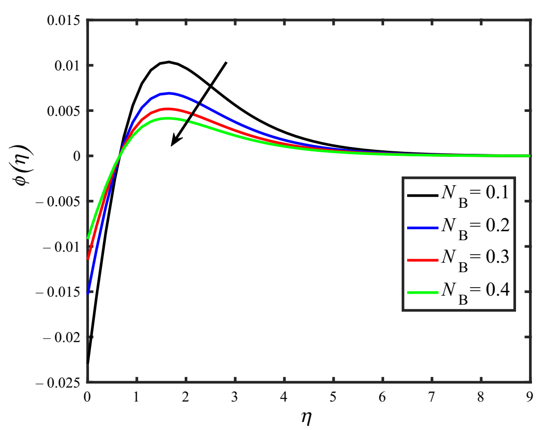

Fig. 27 Profile of $\phi(\eta)$ against N_B

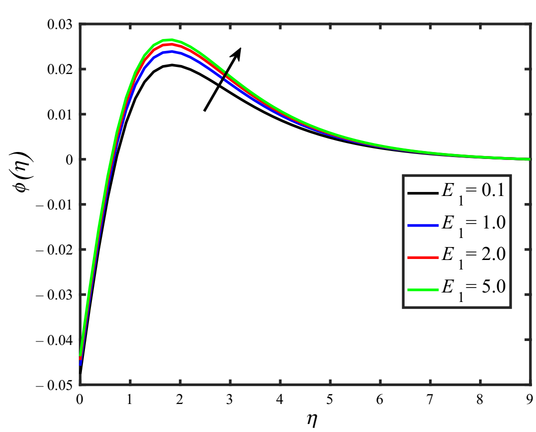

Fig. 28 Profile of $\phi(\eta)$ against E_1

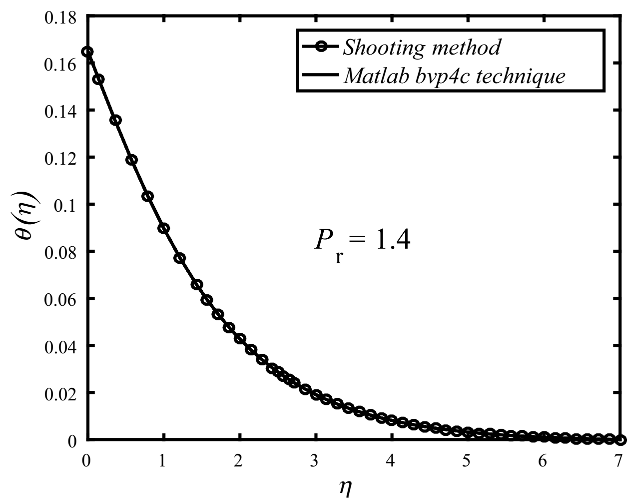

Fig. 29 Comparison of Pr by shooting method

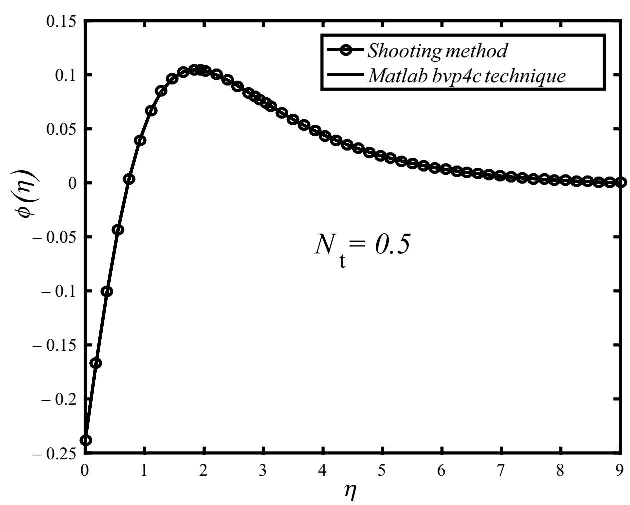

Fig. 30 Comparison of N_T by shooting method

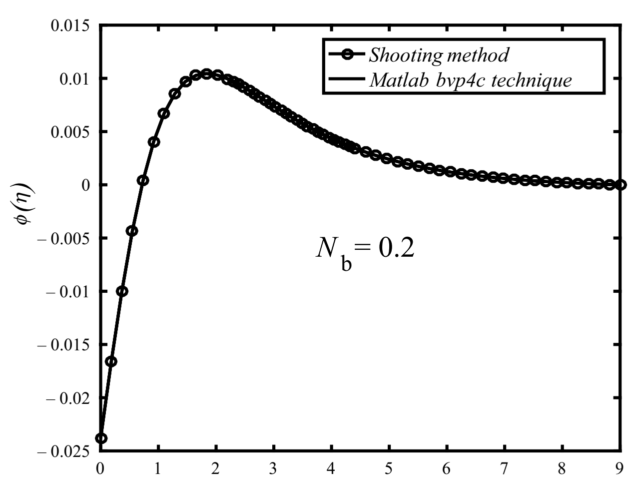

Fig. 31 Comparison of N_B by shooting method

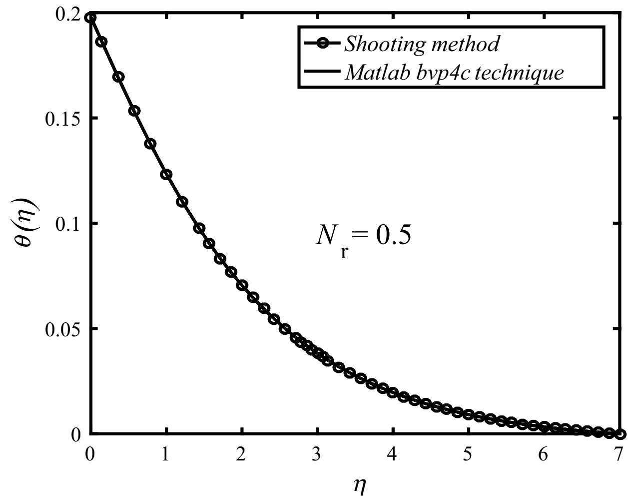

Fig. 32 Comparison of N_r by shooting method

which a rise in S_c yields a drop in concentration. Figure 25 exhibits the effect of relaxation for heat diffusion δ_t on temperature distribution. In Fig. 25, a decrease in temperature against relaxation for heat diffusion δ_t is viewed. The sway of time is for collection diffusion δ_c versus attentiveness profile, which is shown in Fig. 26. The volumetric concentration of nanomaterials is clearly decomposed with an increment in the values of point relaxation for mass diffusion δ_c. The conductivity of Brownian motion parameter on volume friction is plotted in Fig. 27. Escalating N_b results in a decrease in volume friction. Physically, N_b creates a continuous motion between the particles of fluids. This motion enhances chaotic movements, which uplifts the kinetic energy and thus causes the devaluation in the nanoparticle's concentration profiles. Figure 28 elucidates the effect of the Arrhenius activation energy on volumetric concentration profile ϕ. Intensifying the value of parameter E_1, the nanoparticle concentration

Table 3 Statistical shooting assessment and outcomes from bvp4c with Freidoonimehr and Rahimi [75] and Wang [76] for $f''(0)$, when $\gamma = M = 0, \delta_t = 0, \delta_c = 0, Q = 0$ also all extended parameters are zero

Parameter	Ref [47]	Ref [48]	Ref [49]	Shooting	BVP4C
λ	$-f''(0)$	$-f''(0)$	$-f''(0)$	$-f''(0)$	$-f''(0)$
0	1.0000	1.0000	1.0000	1.0000	1.0000
0.25	1.048813	1.048813	1.048812	1.048834	1.048834
0.5	1.093097	1.093095	1.093095	1.093105	1.093105
0.75	1.134485	1.134485	1.134485	1.134491	1.134491
1.0	1.173720	1.173721	1.173721	1.173723	1.173723

Table 4 Statistical shooting assessment and outcomes from bvp4c with Freidoonimehr and Rahimi [75] and Wang [76] for $-g''(0)$ when $\gamma = M = 0, \delta_t = 0, \delta_c = 0, Q = 0$ also all extended parameters are zero

Parameter	Ref [47]	Ref [48]	Ref [49]	Shooting	BVP4C
λ	$-g''(0)$	$-g''(0)$	$-g''(0)$	$-g''(0)$	$-g''(0)$
0	0	0	0	0	0
0.25	0.194564	0.194564	0.194564	0.194564	0.194564
0.5	0.465205	0.465205	0.465205	0.465213	0.465213
0.75	0.794622	0.794622	0.794622	0.794623	0.794623
1.0	1.173720	1.173720	1.173720	1.173720	1.173720

Table 1 Statistical shooting assessment and outcomes from bvp4c with Hayat et al. [72] and Freidoonimehr and Rahimi [75] for $f''(0)$ when $\gamma = M = 0, \delta_t = 0, \delta_c = 0, Q = 0$ also all extended parameters are zero

Parameters		Ref [33]	Ref [34]	Ref [35]	Shooting	BVP4C
M	λ	$-f''(0)$	$-f''(0)$	$-f''(0)$	$-f''(0)$	$-f''(0)$
0	0	1.0000	1.0000	1.0000	1.0000	1.0000
1.0	0	1.414213	1.414214	1.414213	1.414213	1.414213
0	0.5	1.093095	1.093095	1.093095	1.093095	1.093095
1.0	0.5	1.476770	1.476770	1.476770	1.476770	1.476770
0	1.0	1.173721	1.173722	1.173721	1.173723	1.173723
1.0	1.0	1.535710	–	1.535710	1.535710	1.535710

Table 2 Statistical shooting assessment and outcomes from bvp4c with Hayat et al. [72] and Freidoonimehr and Rahimi [75] for $-g''(0)$ when $\gamma = M = 0, \delta_t = 0, \delta_c = 0, Q = 0$ also all extended parameters are zero

Parameters		Ref [47]	Ref [48]	Ref [49]	Shooting	BVP4C
M	λ	$-g''(0)$	$-g''(0)$	$-g''(0)$	$-g''(0)$	$-g''(0)$
0	0	0	0	0	0	0
1.0	0	0	0	0	0	0
0	0.5	0.465205	0.465205	0.465205	0.465213	0.465213
1.0	0.5	0.679809	0.679809	0.679809	0.679809	0.679809
0	1.0	1.173721	1.173721	1.173721	1.173723	1.173723
1.0	1.0	1.535710	–	1.535710	1.535710	1.535710

Table 5 Local Nusselt number $-\theta(0)$ versus $\mathrm{Pr}, \delta_T, \delta_E, \theta_w, N_r, \gamma, N_t, N_b, Q$

Pr	δ_T	δ_E	θ_w	N_r	γ	N_t	N_b	Q	$-\theta'(0)$
1.2	0.1	1.0	0.3	0.5	2.0	0.3	0.2	0.5	0.3075
1.5									0.3558
1.8									0.3997
2.0	0.5	1.0	0.3	0.5	2.0	0.3	0.2	0.5	0.3833
	1.0								0.3631
	1.5								0.3432
2.0	0.1	0.1	0.3	0.5	2.0	0.3	0.2	0.5	0.3608
		0.5							0.3511
		1.0							0.3388
2.0	0.1	1.0	1.5	0.5	2.0	0.3	0.2	0.5	0.3529
			1.6						0.3297
			1.7						0.3034
2.0	0.1	1.0	0.3	0.1	2.0	0.3	0.2	0.5	0.5090
				0.4					0.4444
				0.8					0.3820
2.0	0.1	1.0	0.3	0.5	1.2	0.3	0.2	0.5	0.3742
					1.5				0.3988
					1.8				0.4169
2.0	0.1	1.0	0.3	0.5	2.0	0.1	0.2	0.5	0.4314
						0.5			0.4219
						0.8			0.4147
2.0	0.1	1.0	0.3	0.5	2.0	0.3	0.4	0.5	0.4247
							0.5		0.4267
							0.8		0.4277
2.0	0.1	1.0	0.3	0.5	2.0	0.3	0.2	0.0	0.4289
								1.0	0.4332
								1.0	0.4405

Table 6 Local Sherwood number $-\phi'(0)$ versus $\mathrm{Pr}, \delta_T, \delta_E, E, N_r, \gamma, N_t, N_b$

Pr	δ_T	δ_E	E	N_r	γ	N_t	N_b	$\phi'(0)$
1.2	0.1	1.0	0.1	0.5	2.0	0.3	0.2	0.4612
1.5								0.5331
1.8								0.5996
2.0	0.5	1.0	0.1	0.5	2.0	0.3	0.2	0.3681
	1.0							0.3604
	1.5							0.3569
2.0	0.1	0.1	0.1	0.5	2.0	0.3	0.2	0.4454
		0.5						0.5467
		1.0						0.6481
2.0	0.1	1.0	0.2	0.5	2.0	0.3	0.2	0.6400
			1.0					0.6402
			2.0					0.6403
2.0	0.1	1.0	0.1	0.1	2.0	0.3	0.2	0.7635
				0.4				0.6665
				0.8				0.5731
2.0	0.1	1.0	0.1	0.5	1.2	0.3	0.2	0.5613
					1.5			0.5981
					1.8			0.6254
2.0	0.1	1.0	0.1	0.5	2.0	0.1	0.2	0.2157
						0.5		1.0547
						0.8		1.6581
2.0	0.1	1.0	0.1	0.5	2.0	0.3	0.4	1.2800
							0.5	0.2560
							0.8	0.1600

profiles rise. From Figs. 29–32, it is perceived that on top of the dimensionless rapidity components, heat distribution and the volumetric application profile give a good agreement of shooting technique and the bvp4c technique. A dual comparison is also presented in Tables 1–4 in which firstly the values of different parameters against existing reported results are taken into account and secondly it has been prepared in between two different techniques. It can easily be seen that our applied numerical scheme has produced exactly the same results with the existing shooting technique. An excellent agreement is established when a comparison has been made between current analysis and available results [47–49, 72, 75]. In Tables 1 and 3, the values of $-f''(0)$ are provided against parameters M and λ, while Tables 2 and 4 give the insight into values of same parameters when produced against $-g''(0)$. Additionally, some new results of local Nusselt number and Sherwood number for different physical parameters are also reported in Tables 5 and 6, respectively. It is analyzed that local Nusselt number $-\theta'(0)$ rises with $\mathrm{Pr}, \gamma, N_\mathrm{b}, Q$, but it diminishes with $\delta_\mathrm{T}, \delta_\mathrm{E}, N_\mathrm{T}$. The basic purpose of Table 6 is to represent the various impacts of the key parameters $\mathrm{Pr}, \delta_\mathrm{T}, \delta_\mathrm{E}, \gamma, N_\mathrm{T}, N_\mathrm{b}$ on Sherwood number $\phi'(0)$. As for increasing values of N_T, E, γ getting the higher variation in $\phi'(0)$, the negative behavior is observed for the cases of $N_\mathrm{r}, N_\mathrm{b}$

Conclusions

The quantitative findings of this study are as follows:

- Velocity decreases with higher values of magnetic parameter because of Lorentz forces, whereas temperature boosts up.
- Velocity and concentration decrease with higher values of slip parameter; however, the reverse conductivity is noted for temperature distribution.
- Velocity, temperature and concentration decline with rising values of stretching parameter.
- Enhancement of radiation parameter leads to enhancement of volume friction.
- The temperature distribution decreases with relaxation heat diffusion.

References

1. Rashidi S, Javadi P, Esfahani JA. Second law of thermodynamics analysis for nanofluid turbulent flow inside a solar heater with the ribbed absorber plate. J Therm Anal Calorim. 2019;135(1):551–63.
2. Shamsabadi H, Rashidi S, Esfahani JA. Entropy generation analysis for nanofluid flow inside a duct equipped with porous baffles. J Therm Anal Calorim. 2019;35(2):1009–19.
3. Maleki H, Safaei MR, Togun H, Dahari M. Heat transfer and fluid flow of pseudo-plastic nanofluid over a moving permeable plate with viscous dissipation and heat absorption/generation. J Therm Anal Calorim. 2019;135(3):1643–54.
4. Khan A, Ali HM, Nazir R, Ali R, Munir A, Ahmad B, Ahmad Z. Experimental investigation of enhanced heat transfer of a car radiator using ZnO nanoparticles in H_2O–ethylene glycol mixture. J Therm Anal Calorim. 2019;138(5):3007–21.
5. Szilagyi IM, Santala E, Heikkilä M, Kemell M, Nikitin T, Khryashchev L, Rasanen M, Ritala M, Leskelä M. Thermal study on electrospun polyvinylpyrrolidone/ammonium metatungstate nanofibers: optimising the annealing conditions for obtaining WO_3 nanofibers. J Therm Anal Calorim. 2011;105:73–81.
6. Khan LA, Reza M, Mir NA, Ellahi R. Effects of different shapes of nanoparticles on peristaltic flow of MHD nanofluids filled in an asymmetric channel. J Therm Anal Calorim. 2019. https://doi.org/10.1007/s10973-019-08348-9.
7. Alamri SZ, Ellahi R, Shehzad N, Zeeshan A. Convective radiative plane Poiseuille flow of nanofluid through porous medium with slip: an application of Stefan blowing. J Mol Liq. 2019;273:292–304.
8. Hassan M, Marin M, Ellahi R, Alamri SZ. Exploration of convective heat transfer and flow characteristics synthesis by Cu–Ag/water hybrid-nanofluids. Heat Transf Res. 2018;49(18):1837–48.
9. Laein RP, Rashidi S, Esfahani JA. Experimental investigation of nanofluid free convection over the vertical and horizontal flat plates with uniform heat flux by PIV. Adv Powder Technol. 2016;27:312–22.
10. Ellahi R, Alamri SZ, Basit A, Majeed A. Effects of MHD and slip on heat transfer boundary layer flow over a moving plate based on specific entropy generation. J Taibah Univ Sci. 2018;12(4):476–82.
11. Bovand M, Rashidi S, Esfahani JA. Optimum interaction between magnetohydrodynamics and nanofluid for thermal and drag management. J Thermophys Heat Transf. 2016;31:218–29.
12. Maleki H, Alsarraf J, Moghanizadeh A, Hajabdollahi H, Safaei MR. Heat transfer and nanofluid flow over a porous plate with radiation and slip boundary conditions. J Central South Univ. 2019;26(5):1099–115.
13. Nasiri H, Jamalabadi MYA, Sadeghi R, Safaei MR, Nguyen TK, Shadloo MS. A smoothed particle hydrodynamics approach for numerical simulation of nanofluid flows. J Therm Anal Calorim. 2019;135(3):1733–41.
14. Kamalgharibi M, Hormozi F, Zamzamian SAH, Sarafraz MM. Experimental studies on the stability of CuO nanoparticles dispersed in different base fluids: influence of stirring, sonication and surface active agents. Heat Mass Transf. 2016;52(1):55–62.
15. Salari E, Peyghambarzadeh SM, Sarafraz MM, Hormozi F. Boiling thermal performance of TiO_2 aqueous nanofluids as a coolant on a disc copper block. Periodica Polytech Chem Eng. 2016;60(2):106–12.
16. Sarafraz MM, Hormozi F. Convective boiling and particulate fouling of stabilized CuO–ethylene glycol nanofluids inside the annular heat exchanger. Int Commun Heat Mass Transf. 2014;53:116–23.
17. Sarafraz MM, Hormozi F. Pool boiling heat transfer to dilute copper oxide aqueous nanofluids. Int J Therm Sci. 2015;90:224–37.
18. Majeed A, Zeeshan A, Bhatti MM, Ellahi R. Heat transfer in magnetite (Fe_3O_4) nanoparticles suspended with conventional fluids: refrigerant-134a ($C_2H_2F_4$), kerosene ($C_{10}H_{22}$) and water (H_2O) under the impact of dipole. Heat Transf Res. 2020;51(3):217–32.
19. Hassan A, Wahab A, Qasim MA, Janjua MM, Ali MA, Ali HM, Jadoon TR, Ali E, Raza A, Javaid N. Thermal management and

uniform temperature regulation of photovoltaic modules using hybrid phase change materials-nanofluids system. Renew Energy. 2020;145:282–93.
20. Ambreen T, Saleem A, Ali HM, Shehzad SA, Park CW. Performance analysis of hybrid nanofluid in a heat sink equipped with sharp and streamlined micro pin-fins. Powder Technol. 2019;355:552–63.
21. Choi SUS, Eastman JA. Enhancing thermal conductivity of fluid with nanoparticles. In: Conference: 1995 international mechanical engineering congress and exhibition, San Francisco, CA, 1995, p. 12–17.
22. Boungiorno J, Hu LW, Kim SJ, Hannink R, Truong B, Forrest E. Nanofluids for enhanced economics and safety of nuclear reactors: an evaluation of potential features, issues, and research gaps. Nucl Technol. 2008;162:80–91.
23. Powell RE, Eyring H. Mechanisms for the relaxation theory of viscosity. Nature. 1944;154:427–8.
24. Patel M, Timol MG. Numerical treatment of Powell–Eyring fluid flow using method of satisfaction of asymptotic boundary conditions (MSABC). Appl Numer Math. 2009;59:84–92.
25. Hayat T, Abbas Z, Qasim M, Obidet S. Steady flow of an Eyring Powell fluid over a moving surface with convective boundary condition. Int J Heat Mass Transf. 2012;8:17–22.
26. Akbar NS, Ebraid A, Khan ZH. Numerical analysis of magnetic field effects on Eyring–Powell fluid flow towards a stretching sheet. J Magn Magn Mater. 2015;382:355–8.
27. Hayat T, Hussain Z, Farooq M, Alsaedi A. Magnetohydrodynamic flow of Powell–Eyring fluid by a stretching cylinder with Newtonian heating. Therm Sci. 2018;22:371–82.
28. Ellahi R. The effects of MHD and temperature dependent viscosity on the flow of non-Newtonian nanofluid in a pipe: analytical solutions. Appl Math Model. 2013;37(3):1451–7.
29. Alamri SZ, Khan AA, Azeez M, Ellahi R. Effects of mass transfer on MHD second grade fluid towards stretching cylinder: a novel perspective of Cattaneo–Christov heat flux model. Phys Lett A. 2019;383:276–81.
30. Ellahi R, Zeeshan A, Hussain F, Abbas T. Thermally charged MHD bi-phase flow coatings with non-Newtonian nanofluid and Hafnium particles through slippery walls. Coatings. 2019;9:300.
31. Ellahi R, Zeeshan A, Hussain F, Abbas T. Two-phase Couette flow of Couple stress fluid with temperature dependent viscosity thermally affected by magnetized moving surface. Symmetry. 2019;11(5):647.
32. Ellahi R, Hussain F, Ishtiaq F, Hussain A. Peristaltic transport of Jeffrey fluid in a rectangular duct through a porous medium under the effect of partial slip: an approach to upgrade industrial sieves/filters. Pramana. 2019;93:34.
33. Khan AA, Bukhari SR, Marin M, Ellahi R. Effects of chemical reaction on third grade magnetohydrodynamics fluid flow under the influence of heat and mass transfer with variable reactive index. Heat Transf Res. 2019;50(11):1061–80.
34. Ellahi R, Sait SM, Shehzad N, Mobin N. Numerical simulation and mathematical modeling of electro-osmotic Couette–Poiseuille flow of MHD power-law nanofluid with entropy generation. Symmetry. 2019;11:1038.
35. Maleki H, Safaei MR, Alrashed AAAA, Kasaeian A. Flow and heat transfer in non-Newtonian nanofluids over porous surfaces. J Therm Anal Calorim. 2019;135:1655–66.
36. Eldabe NT, Hassan AA, Mohamed MA. Effect of couple stresses on the MHD of a non-Newtonian unsteady flow between two parallel porous plates. Zeitschrift für Naturforschung A. 2003;58:204–10.
37. Malik MY, Bilal S, Bibi M, Ali U. Logarithmic and parabolic curve fitting analysis of dual stratified stagnation point MHD mixed convection flow of Eyring–Powell fluid induced by an inclined cylindrical stretching surface. Results Phys. 2017;7:544–52.
38. Islam S, Shah A, Zhou CY, Ali I. Homotopy perturbation analysis of slider bearing with Powell–Eyring fluid. Z Angew Math Phys. 2009;60:1178.
39. Akbar NS, Nadeem S. Characteristics of heating scheme and mass transfer on the peristaltic flow for an Eyring–Powell fluid in an endoscope. Int J Heat Mass Transf. 2012;55:375–83.
40. Sirohi V, Timol MG, Kalthia NL. Powell–Eyring model flow near an accelerated plate. Fluid Dyn Res. 1987;2(3):193–204.
41. Nadeem S, Akbar NS, Ali M. Endoscopic effects on the peristaltic flow of an Eyring–Powell fluid. Meccanica. 2012;47(3):687–97.
42. Jayachandra Babu M, Sandeep N, Raju CS. Heat and mass transfer in MHD Eyring–Powell nanofluid flow due to cone in porous medium. Int J Eng Res Afr. 2016;19:57–74.
43. Yoon HK, Ghajar AJ. A note on the Powell–Eyring fluid model. Int Commun Heat Mass Transf. 1987;14(4):381–90.
44. Agbaje TM, Mondal S, Motsa SS, Sibanda P. A numerical study of unsteady non-Newtonian Powell–Eyring nanofluid flow over a shrinking sheet with heat generation and thermal radiation. Alex Eng J. 2017;56(1):81–91.
45. Gailitis A, Lielausis O. On the possibility to reduce the hydrodynamic drag of a plate in an electrolyte. Appl Magnetohydrodyn Rep Phys Inst Riga. 1961;12:143–6.
46. Ahmad R, Mustafa M, Turkyilmazoglu M. Buoyancy effects on nanofluid flow past a convectively heated vertical Riga-plate: a numerical study. Int J Heat Mass Transf. 2017;111:827–35.
47. Iqbal Z, Mehmood Z, Azhar E, Maraj EN. Numerical investigation of nanofluidic transport of gyrotactic microorganisms submerged in water towards Riga plate. J Mol Liq. 2017;234:296–308.
48. Khan NA, Aziz S, Khan NA. MHD flow of Powell–Eyring fluid over a rotating disk. J Taiwan Inst Chem Eng. 2014;45(6):2859–67.
49. Makinde OD, Aziz A. Boundary layer flow of a nanofluid past a stretching sheet with a convective boundary condition. Int J Therm Sci. 2011;50(7):1326–32.
50. Goodarzi M, Safaei MR, Vafai K, Ahmadi G, Dahari M, Kazi SN, Jomhari N. Investigation of nanofluid mixed convection in a shallow cavity using a two-phase mixture model. Int J Therm Sci. 2014;75:204–20.
51. Riaz A, Ellahi R, Bhatti MM, Marin M. Study of heat and mass transfer in the Eyring–Powell model of fluid propagating peristaltically through a rectangular complaint channel. Heat Transf Res. 2019;50(16):1539–60.
52. Gireesha BJ, Gorla RS, Mahanthesh B. Effect of suspended nanoparticles on three-dimensional MHD flow, heat and mass transfer of radiating Eyring–Powell fluid over a stretching sheet. J Nanofluids. 2015;4(4):474–84.
53. Hayat T, Muhammad T, Shehzad SA, Alsaedi A. Similarity solution to three dimensional boundary layer flow of second grade nanofluid past a stretching surface with thermal radiation and heat source/sink. AIP Adv. 2015;5(1):017107.
54. Hayat T, Muhammad T, Shehzad SA, Alsaedi A. Three-dimensional boundary layer flow of Maxwell nanofluid. J Mol Liq. 2017;229:495–500.
55. Hedayati F, Malvandi A, Kaffash MH, Ganji DD. Fully developed forced convection of alumina/water nanofluid inside microchannels with asymmetric heating. Powder Technol. 2015;269:520–31.
56. Fukui S, Kaneko R. A database for interpolation of Poiseuille flow rates for high Knudsen number lubrication problems. J Tribol. 1990;112(1):78–83.
57. Maxwell JC. On stresses in rarified gases arising from inequalities of temperature. Philos Trans R Soc Lond. 1879;170:231–56.
58. Mitsuya Y. Modified Reynolds equation for ultra-thin film gas lubrication using 1.5-order slip-flow model and considering surface accommodation coefficient. J Tribol. 1993;115(2):289–94.

59. Hsia YT, Domoto GA, Hsia YT, Domoto GA. An experimental investigation of molecular rarefaction effects in gas lubricated bearings at ultra-low clearances. J Tribol. 1983;105:120–30.
60. Maleque K. Effects of exothermic/endothermic chemical reactions with Arrhenius activation energy on MHD free convection and mass transfer flow in presence of thermal radiation. J Thermodyn. 2013;2013:692516.
61. Zhang J, Li Y, Xie J. Numerical simulation of fractional control system using Chebyshev polynomials. Math Probl Eng. 2018;2018:4270764.
62. Shafique Z, Mustafa M, Mushtaq A. Boundary layer flow of Maxwell fluid in rotating frame with binary chemical reaction and activation energy. Results Phys. 2016;6(1):627–33.
63. Hemeda AA, Eladdad EE. New iterative methods for solving Fokker–Planck equation. Math Probl Eng. 2018;2018:6462174.
64. Asadollahi A, Esmaeeli A. Simulation of condensation and liquid break-up on a micro-object with upper and lower movable walls using Lattice Boltzmann method. Physica A. 2018;498:33–49.
65. Rashidi S, Akbarzadeh M, Karimi N, Masoodi R. Combined effects of nanofluid and transverse twisted-baffles on the flow structures heat transfer and irreversibilities inside a square duct—a numerical study. Appl Therm Eng. 2018;130:135–48.
66. Ellahi R, Sait SM, Shehzad N, Ayaz Z. A hybrid investigation on numerical and analytical solutions of electro-magnetohydrodynamics flow of nanofluid through porous media with entropy generation. Int J Numer Meth Heat Fluid Flow. 2020;30(2):834–54.
67. Nikkhah V, Sarafraz MM, Hormozi F, Peyghambarzadeh SM. Particulate fouling of CuO–water nanofluid at isothermal diffusive condition inside the conventional heat exchanger-experimental and modeling. Exp Therm Fluid Sci. 2015;60:83–95.
68. Khan JA, Mustafa M, Hayat T, Alsaedi A. Numerical study of Cattaneo–Christov heat flux model for viscoelastic flow due to an exponentially stretching surface. PLoS ONE. 2015;10:0137363.
69. Nadeem S, Muhammad N. Impact of stratification and Cattaneo–Christov heat flux in the flow saturated with porous medium. J Mol Liq. 2016;224:423–30.
70. Hayat T, Zubair M, Waqas M, Alsaedi A, Ayub M. On doubly stratified chemically reactive flow of Powell–Eyring liquid subject to non-Fourier heat flux theory. Results Phys. 2017;7:99–106.
71. Salahuddin T, Malik MY, Hussain A, Bilal S, Awais M. MHD flow of Cattanneo–Christov heat flux model for Williamson fluid over a stretching sheet with variable thickness: using numerical approach. J Magn Magn Mater. 2016;401:991–7.
72. Hayat T, Ali Shehzad S, Qasim M, Asghar S. Three-dimensional stretched flow via convective boundary condition and heat generation/absorption. Int J Numer Methods Heat Fluid Flow. 2014;24(2):342–58.
73. Hayat T, Muhammad T, Alsaedi A, Ahmad B. Three-dimensional flow of nanofluid with Cattaneo–Christov double diffusion. Results Phys. 2016;6:897–903.
74. Umar M, Akhtar R, Sabir Z, Wahab HA, Zhiyu Z, Imran A, Shoaib M, Raja MAZ. Numerical treatment for the three-dimensional Eyring–Powell fluid flow over a stretching sheet with velocity slip and activation energy. Adv Math Phys. 2019;2019:9860471.
75. Freidoonimehr N, Rahimi AB. Brownian motion effect on heat transfer of a three-dimensional nanofluid flow over a stretched sheet with velocity slip. J Therm Anal Calorim. 2019;135(1):207–22.
76. Wang CY. The three dimensional flow due to a stretching flat surface. Phys Fluids. 1984;27(8):1915.